Journal of Controlled Release 342 (2022) 157–169

Contents lists available at ScienceDirect

Journal of Controlled Release

journal homepage: www.elsevier.com/locate/jconrel

Organic NIR-II dyes with ultralong circulation persistence for image-guided delivery and therapy

Yang Li [a,b,e,1], Jianfeng Gao [a,d,1], Shuping Wang [c,1], Shijun Li [c], Xiaowen Hou [a], Yanna Pan [a], Jialu Gao [a], Xue Qiao [b], Zhiquan Tian [b], Deliang Chen [f], Hai Deng [g], Zixin Deng [a,b], Xuechuan Hong [a,b], Yuling Xiao [a,e,*]

[a] State Key Laboratory of Virology, Hubei Province Engineering and Technology Research Center for Fluorinated Pharmaceuticals and Key Laboratory of Combinatorial Biosynthesis and Drug Discovery (MOE), Wuhan University School of Pharmaceutical Sciences, Wuhan 430071, China
[b] College of Science, Research Center for Ecology, Laboratory of Extreme Environmental Biological Resources and Adaptive Evolution, Tibet University, Lhasa 850000, China
[c] College of Material, Chemistry and Chemical Engineering, Hangzhou Normal University, Hangzhou 311121, China
[d] ABSL-III Laboratory at the Center for Animal Experiment, Wuhan University, Wuhan 430071, China
[e] Shenzhen Institute of Wuhan University, Shenzhen 518057, China
[f] Jiangxi Key Laboratory of Organo-Pharmaceutical Chemistry, Chemistry and Chemical Engineering College, Gannan Normal University, Ganzhou, Jiangxi 341000, PR China
[g] Department of Chemistry, University of Aberdeen, Aberdeen, UK

ARTICLE INFO

Keywords:
Drug delivery
Image-guided therapy
Second near-infrared window (NIR-II)
Self-assembly
Fluorescence imaging

ABSTRACT

Nanocarriers hold great promise for the controlled release of therapeutic payloads to target organs/tissues and extended duration of anticancer agents in the bloodstream. However, limited data on their *in vivo* pharmacokinetics and delivery process hamper clinical applications. Here we report a series of micellar nanocarriers self-assembled from new-generation thiophenthiadiazole (TTD)-based NIR-II fluorophores **HLAnP** (n = 1–4) for simultaneous bioimaging and drug delivery. The NIR-II **HLA4P** nanocarrier displays exceptional non-fouling performance, minimal immunogenicity, ultralong blood half-life, and high tumor accumulation even with different administration routes. When used as a drug carrier, **HLA4P** with encapsulated doxorubicin (DOX) realized accurate tumor targeting and continuous real-time *in vivo* NIR-II tracking of drug delivery and therapy, showing a sustained release rate, improved therapeutic effect, and diminished cardiotoxicity as compared to free DOX. This study provides a new perspective on the design of dual-functional NIR-II fluorophores for diagnostic and therapeutic applications.

1. Introduction

The death rate for many cancers has decreased over recent decades due to a better understanding of cancer biology as well as new methods of diagnosis and treatment [1–5]. Conventional chemotherapy by utilizing anticancer drugs to inhibit the growth and division of cancer cells is a mainstay of cancer treatment [6–9]. However, most anticancer drugs are nonselective and incapable of accumulating in tumor tissues [10–12]. Due to the risk of damaging healthy normal tissues and organs, chemotherapeutics are often administered at high doses to improve therapeutic efficacy, but can still be followed by recurrence of cancer and drug resistance [13–15]. In order to improve the efficacy and/or mitigate side effects, a variety of novel drug delivery systems including liposomes [16], polymers, protein-based nanocarriers [17], micelles [18–20], hydrogels, and inorganic nanocarriers [21] have been developed for cancer treatment, leveraging the active cellular uptake and enhanced permeability and retention (EPR) effect [22–26]. Nevertheless, specific antibodies can still be generated under *in vivo* immune conditions because of the nonspecific interaction between nanomaterials and highly immunogenic proteins [24,27]. Therefore, reducing or eliminating nonspecific biomolecules and cellular absorption is of paramount importance to the safety and correct functioning of

* Corresponding author at: State Key Laboratory of Virology, Hubei Province Engineering and Technology Research Center for Fluorinated Pharmaceuticals and Key Laboratory of Combinatorial Biosynthesis and Drug Discovery (MOE), Wuhan University School of Pharmaceutical Sciences, Wuhan 430071, China.
E-mail address: xiaoyl@whu.edu.cn (Y. Xiao).
[1] These authors contributed equally to this work.

https://doi.org/10.1016/j.jconrel.2022.01.005
Received 25 October 2021; Received in revised form 31 December 2021; Accepted 3 January 2022
Available online 5 January 2022

drug-delivering carriers [28–30].

The therapeutic efficacy of anticancer nanomedicines remains far below expectations, and their *in vivo* pharmacokinetics are still unsatisfactory. Very little is known about the delivery routes of drug carriers in real time after they enter the human body, which has limited clinical translation [31–33]. A few near-infrared fluorophores, such as ICG [34], IR-780 [35], and Cy-7.5 [36] have been widely utilized for labeling drugs or tracking drug absorption, metabolism, distribution, and feedback of therapeutic results. However, the labeling process can change the physical and chemical properties of the original drug, resulting in a large difference between imaging results and the true drug metabolism [31]. Additionally, the modification of nanomedicines with different functional components can also cause difficulties in characterizing *in vivo* behaviors, and establishing a standard production procedure in accordance with good manufacturing practices (GMP) [37]. Therefore, a distinct design strategy for organic fluorescent drug carriers with long blood circulation and high tumor affinity for therapeutic delivery is highly desirable.

Compared with visible (450–600 nm) and NIR-I (650–900 nm) light, fluorescence imaging in the near-infrared-II windows (NIR-II, 1000–1700 nm) and sub-windows (NIR-IIa, 1300–1400 nm; NIR-IIb, 1500–1700 nm) has attracted growing attention because of dramatically diminished scattering and photon absorption as well as tissue autofluorescence, resulting in unparalleled spatiotemporal resolution and tissue penetration [38–40]. NIR-II fluorophores, including single-walled carbon nanotubes (SWCNTs) [41], rare-earth-doped nanoparticles (RENPs) [42,43], quantum dots (QDs) [44,45], organic fluorophores (OFs) [46,47], conjugated polymers (CPs) [48,49], and gold nanoclusters (AuNCs) [50] have been widely employed for cancer theranostics. PEGylated small-molecule NIR-II fluorophores such as **CH1055-PEG$_n$** [51,52], IR-BEMC6P [53], and IR-BGP6 [54] are susceptible to rapid clearance, which limits both tumor accumulation and tumor retention time (0–48 h) (Fig. 1). However, the alkyl chain can be integrated into the backbone of fluorescent molecules to enhance self-assembly [55], improve quantum yield (QY) [56], and prolong blood circulation time of drugs for diabetes [57]. Prolonging the circulation time in the blood increases the likelihood that circulating nanocarriers will encounter and act upon the targets of interest. Thus, we further hypothesize that the alkyl and PEG chains are integrated into a novel NIR-II organic fluorescent platform that can self-assemble into a

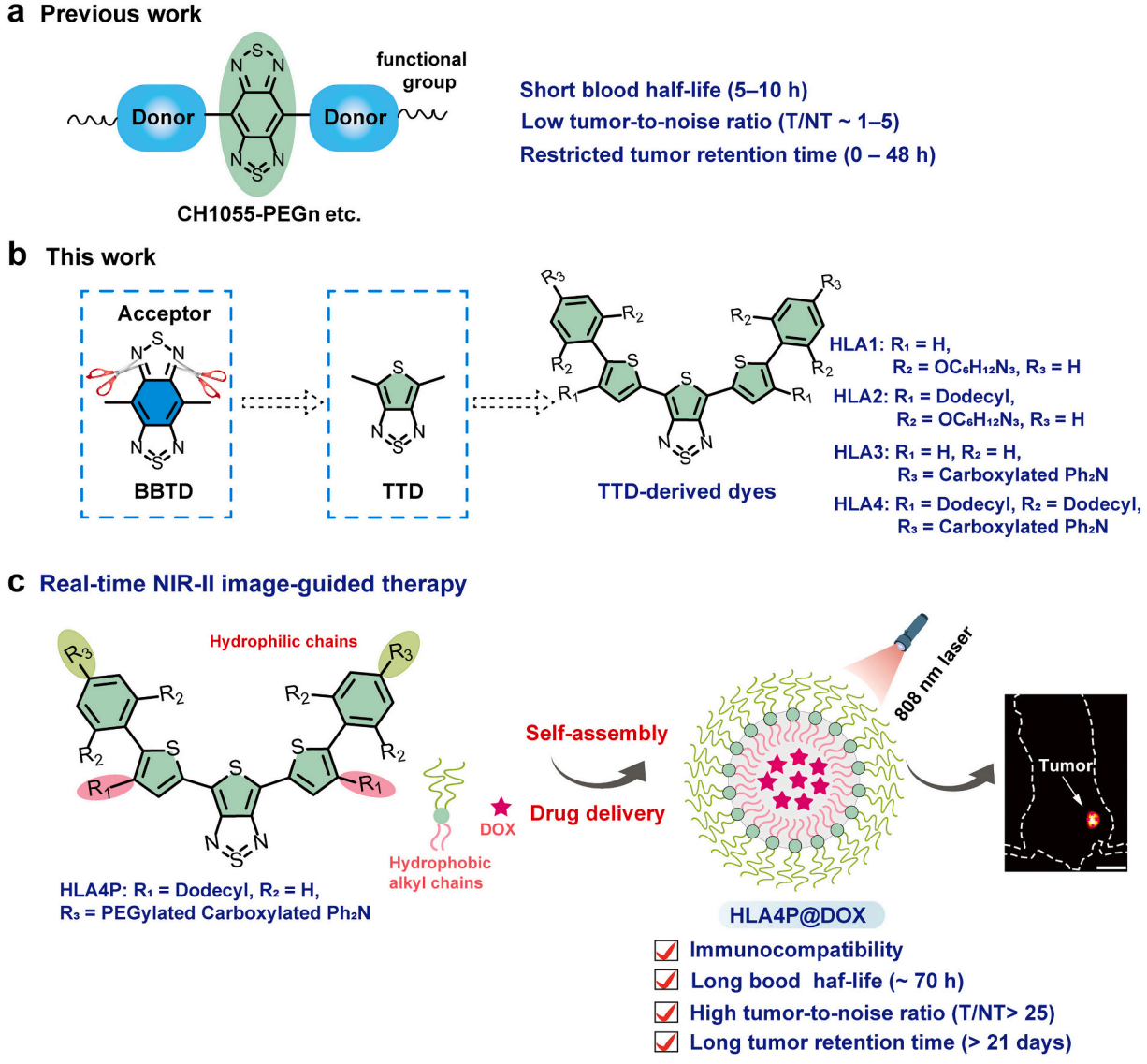

Fig. 1. Design of TTD-derived fluorophore **HLA4P** for therapeutic delivery and image-guided therapy. (a) Typical PEGylated BBTD-derived NIR-II probes. (b) Rational design of NIR-II fluorescence molecules **HLA4** based on TTD acceptor core. (c) Amphiphilic molecule **HLA4P** used for drug delivery and image-guided therapy.

nanoprobe to reduce or eliminate undesirable "biofouling" with long blood circulation time as drug carriers.

In this study, we utilized small-molecule NIR-II fluorophores as novel trackable drug carriers, and morphology-controlling templates for therapeutic delivery and image-guided therapy (Fig. 1). We are particularly interested in thiophenthiadiazole (TTD) as a novel electron acceptor unit. We engineered and synthesized a series of new-generation thiophenthiadiazole (TTD)-based NIR-II fluorophores **HLAn** (n = 1–4) depending on the density functional theory (DFT) calculation (Fig. 2). The optical bandgap (Egap) of TTD-based fluorophores (1.48 eV–1.77 eV) is close to 1.5 eV, a typical Egap for benzo-bis(1,2,5-thiadiazole) (BBTD)-based fluorophores. PEG_{2k} was modified on both sides of **HLAn** (n = 1–4), and the carbon chains on the backbone were extended from C_0 to C_{12}. These PEGylated fluorophores **HLAnP** (n = 1–4) self-

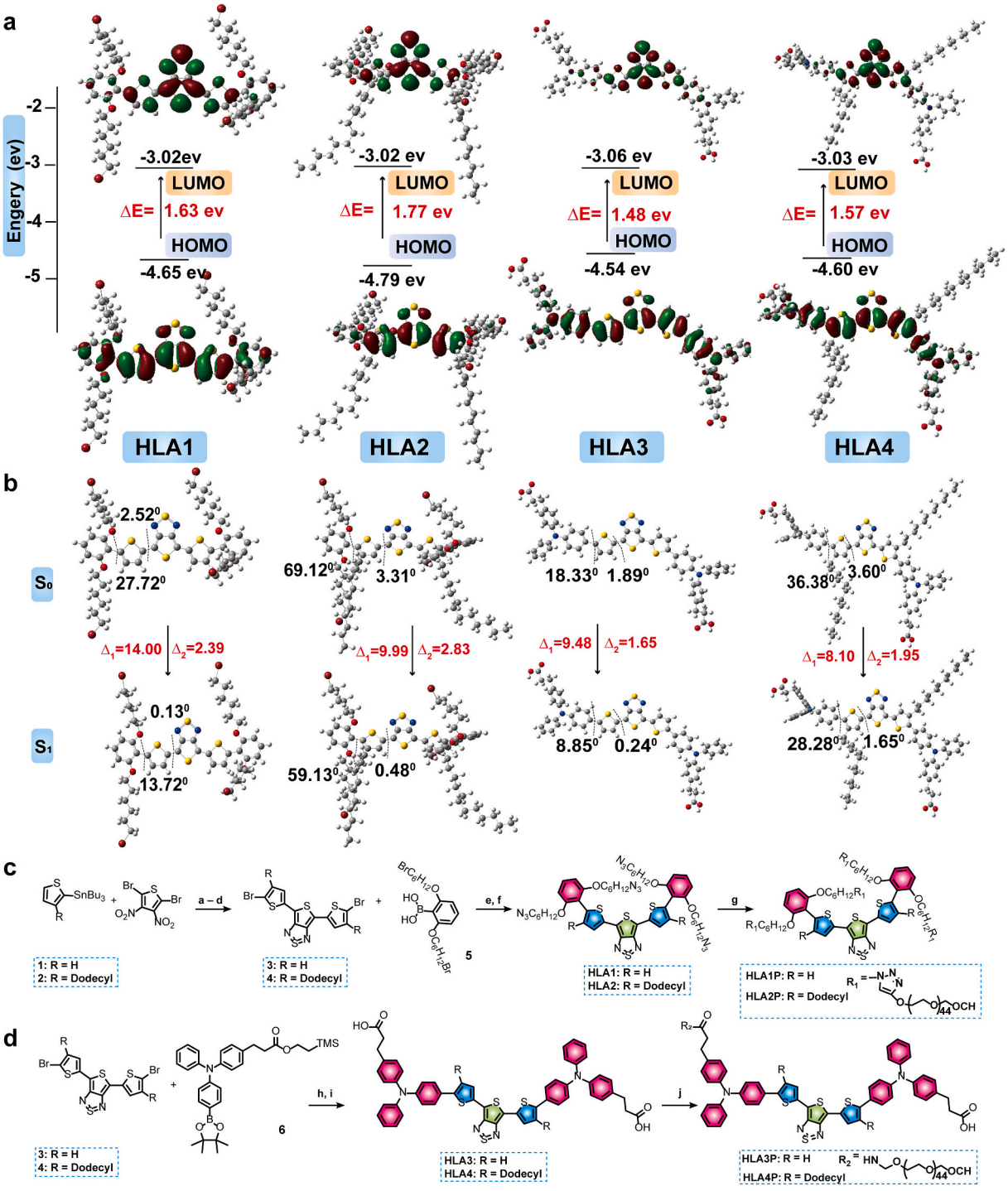

Fig. 2. Density functional theory calculations for TTD-based fluorophores. (a) HOMOs and LUMOs of **HLA1–4** at B3LYP/6-31G(d) scrf method using Gaussian 09 time-dependent density functional theory (TD-DFT) calculations. (b) Optimized S_0 and S_1 geometries of the molecular fluorophores using Gaussian 09 software. (c) and (d) Synthesis of **HLA1–4 and HLA1P–4P**. Conditions and reagents: a) $Pd(PPh_3)_4$, tributyl(4-hexylthiophen-2-yl)stannane, toluene, 110 °C, 6 h, 65%–70%; b) Zn powder, NH_4Cl, $MeOH/H_2O$, CH_2Cl_2 25 °C, 2 h; c) PhNSO, pyridine, TMSCl, 25 °C, ~ 50% (two steps); d) pyridine, NBS, 25 °C, 2 h, 90%; e) 14% $NaHCO_3$, $Pd(PPh_3)_4$, THF/H_2O, 75 °C, 6 h, 30%–40.2%; f) NaN_3, DMF, 25 °C, 3 h, 95%; g) PEG_{2K}-alkynyl, TBTA, CuI, THF, 25 °C, 12 h, 85%; h) 15% $NaHCO_3$, $Pd(PPh_3)_4$, THF/H_2O, 75 °C, 4 h, 38%–40%; i) TFA, CH_2Cl_2, 0 °C, 6 h, 98%; j) PEG_{2K}-NH_2, HATU, DIPEA, DMF, 25 °C, 12 h, 56%–73%.

assembled into spherical or vesicular micelles (1–200 nm) with high fluorescence QYs (0.15%–1.3%), exceptional nonfouling performance, and minimal immunogenicity in aqueous solution. Notably, even administered by various routes (intravenous, intraperitoneal, intramuscular, and subcutaneous injection, respectively), **HLA4P** exhibited long circulation life-time *in vivo* ($t_{1/2}$ = 70 h), super-contrast ratio (T/NT > 25), and long tumor retention time (> 3 weeks) through passive targeting with less reticuloendothelial system (RES) uptake. More importantly, **HLA4P** could efficiently encapsulate an anticancer drug doxorubicin (DOX, ~ 65% encapsulation efficiency), and perform sustained release of DOX. **HLA4P@DOX** not only demonstrated bright NIR-II emission (~1035 nm), and tumor retention persisted for 14 days, but also showed improved therapeutic effect and reduced side effects than free DOX *in vitro* and *in vivo*. Specifically, **HLA4P@DOX** could be excited by 808 nm laser, demonstrating the ability for real-time tracking, and continuous *in vivo* NIR-II imaging for a long period of time. These results collectively indicate that, as a novel NIR-II fluorescence probe, **HLA4P** has tremendous potential for accurate preoperative tumor assessment, long-term *in vivo* monitoring, and controlled release of an antitumor drug *in situ* (Fig. 1).

2. Experimental section

2.1. Experimental materials

Polyethylene glycol (PEG) with various molecular weights were purchased from Ponsure Biotechnology Company. Ethyl acetate (EA), petroleum ether (PE), *N*, *N*-Dimethylformamide (DMF), tetrahydrofuran (THF), ethanol dichloromethane (CH_2Cl_2), *etc.* reagents were obtained from Shenshi Chemical Co., Ltd. in Wuhan. PhNSO, EDCI HATU, DMAP, TMSCl, DIPEA, palladium catalyst and inorganic salt *etc.* synthetic reagents were obtained from Leyan, Innochem, Aladdin, Adamas and other reagent companies. Silica gel column chromatography was purchased from Qingdao Marine Chemical Co., Ltd. Water was purified water acquired by a water making mechanism.

2.2. Fluorescence QY measurement

Fluorescent QYs of TTD-derived fluorophores were tested on the basis of the previously reported experimental method [46]. Firstly, five points were chosen between the absorbance values of 0.1–1. The fluorescent intensity was measured based on these five points respectively. The linear relationship was fitted between the integrated fluorescent intensity and the absorbance value *via* the first-order function. The TTD-derived fluorophores' QYs were obtained on the basis of the following formula:

$$QY_{samp} = QY_{refe} \times \frac{S_{samp}}{S_{refe}} \times \left(\frac{n_{samp}}{n_{refe}}\right)^2 \quad (1)$$

QY_{samp} represents the dyes, QY_{refe} represents the IR-26.

2.3. Critical micelle concentration measurement

A solution of **HLAnP** (n = 1–4) at a concentration of 200 μM deionized water was prepared by sonication for half an hour and filtration, respectively. Drops of these aqueous solutions were dropped on carbon-coated grids (Cu, 400 mesh) and then dried for 2 days before TEM photography.

2.4. Tem

The morphology of the **HLAnP** (n = 1–4) was studied by TEM. TEM specimens were prepared by dropping the solution of **HLAnP** onto carbon-coated grids (Cu, 400 mesh) and dried for 2 days.

2.5. Cell experiment and animal models

Mouse breast cancer cells 4 T1, Human liver cells L02, mouse colorectal carcinoma cells CT-26, human glioma cells U87MG cells and human hepatoma cell line HepG2 were obtained from the China Center for Type Culture Collection (CCTCC). HepG2, 4 T1 and U87cells used in the experiments were cultured in Dulbecco's modified Eagle medium (DMEM) medium. CT-26 cells were cultured in 1640 medium. All mice were obtained from SJA Laboratory Animal Co. The fluorescent imaging was performed at 12-days post injection of tumor cells subcutaneously into mice.

2.6. MTT cytotoxicity assay

The cellular viability assessments were performed on the Human liver normal cells (L02) and CT-26 cells. PBS buffer (100 μL) was added to the outermost hole of 96 well plates. The leftover 60 holes were added with a solution of cells (100 μL), and the cells were incubated for 24 h. **HLA4P** solutions with various concentrations were prepared using the culture medium. **HLA4P** containing medium solutions (100 μL) with various concentrations were added. After incubated for 24 h, the 96 well plate was taken out. The medium containing **HLA4P** was removed, and then 100 μL of MTT solution was added respectively. After incubated for 4 h, the MTT solution was removed and 150 μL DMSO was added.

The cell viability of **HLA4P@DOX** and DOX against CT-26 cells was measured for 24 h incubation. The CT-26 cells were cultured on a 96-well plate. After incubated for 48 h, a MTT procedure was conducted to measure the cytotoxicity.

2.7. Blood-half-life determination

HLA4P (200 μL, 200 μM) was injected into the ICR mice (n = 3) *via* intravenous, intraperitoneal, intramuscular and subcutaneous injection, respectively. The blood sample was collected at different time points. Anticoagulant was added into the blood sample to prevent blood clotting. After collecting all the blood samples, the NIR-II fluorescence images were recorded at 200 ms exposure time (808 nm laser, 1000 nm LP filter, 90 mW/cm^2). The integrated fluorescence value of the blood samples was plotted, and the plots were then fitted to a corresponding first order decay exponential function.

2.8. Feces and urine

HLA4P was intravenously injected into the BALB/c mice (n = 5 per group). The feces and urine were obtained at various time points using a metabolic cage. After collecting the feces and urine samples, the NIR-II imaging was conducted at 200 ms (808 nm laser, 1000 nm LP filter).

2.9. NIR-II fluorescent imaging

HLA1P-4P was injected into 4 T1 tumor BALB/c mice or ICR mice. **HLA4P** was administrated into mice through different injection routes. We used the isoflurane to anesthetize the mice. The mice were put in the intravital NIR-II optical imaging system with a prone or supine position. The NIR-II images of whole-body mice post-injection of **HLA1P-4P** were collected. The instrumental specs of intravital NIR-II optical imaging system are using different LP filters with different exposure time under 808 nm laser.

2.10. Biodistribution of *HLAnP*

Ex vivo distribution of **HLAnP** was performed by NIR-II fluorescent intensity. After injection of **HLAnP** for NIR-II imaging, the 4 T1, CT-26, HepG2 and U87MG tumor-bearing mice models (n = 3) were sacrificed, NIR-II fluorescent images of liver, tumor and other organs were acquired. The NIR-II fluorescent signals of various tissues were analyzed

by ImageJ software.

2.11. Preparation of *HLA4P@DOX*

Firstly, free DOC was obtained by neutralization of DOX·HCl. Amphiphilic fluorophore **HLA4P** (5 mg) and free drug DOX (1 mg) were added into a DMSO solution. Deionized water or PBS was added into a rounded-bottom flask, and then a mixture of **HLA4P** and DOX was slowly dropped into a rounded-bottom flask. After the addition, the aforementioned solution was ultrasonicated for 10 s. The mixture solution was dialyzed to remove the free DOX for ~48 h, and the deionized water was changed over 6 times.

2.12. Entrapment efficiency and drug loading content

Different concentrations of DOX in DMSO were performed for a calibration curve. After dialysis, DOX was separated from **HLA4P@DOX** and dissolved in DMSO to determine the absorption wavelength at 480 nm. The drug loading efficiency (DLE) and drug loading content (DLC) were analyzed through the following calculation formulas:

$$\text{DLC}\ (\%) = \frac{\text{weight of DOX in nanoparticles}}{\text{weight of the nanoparticles}} \times 100\% \quad (2)$$

$$\text{DLE}\ (\%) = \frac{\text{weight of DOX in nanoparticles}}{\text{weight of the adding drug}} \times 100\% \quad (3)$$

2.13. Confocal laser scanning

CT-26 cells were incubated in a culture flask. After incubated for 24 h, **HLA4P@DOX** in a medium solution (1 mL) was added. After incubated for additional 4 h, the medium in the small dish was removed, and PBS (1 mL) was added. Each small dish was then added a 4% paraformaldehyde solution (1 mL) for the cell fixation. After 15 min, the paraformaldehyde stationary solution was removed, the cells were washed with PBS buffer three times, and stained with a DAPI solution (200 μL). After 10 min, the DAPI staining solution was also removed, and the cells were washed with PBS buffer three times and observed under the Leica-LCS-SP8-STED instrument.

2.14. Biodistribution of *HLA4P@DOX*

We randomly divided the ICR mice into different groups. **HLA4P@DOX** and free DOX solution were i.v. injected into ICR mice. Blood samples were obtained from various time points, and then whole blood samples were centrifuged at 13000 rpm for 15 min to collect plasma. We randomly divided the CT-26 tumor-bearing Balb/c mice into different groups. **HLA4P@DOX** and free DOX solution were i.v. injected into CT-26 bearing-mice models. The mice were sacrificed at various time points after injection, and then the heart, spleen, liver, lung, kidney, and tumor were acquired and weighed. These plasma and tissues were suspended in a solution of 70% ethanol with 0.3 *N* HCl and then the mixture was intensely homogenized. The absorbance of DOX in the supernatant was measured at 480 nm wavelength after centrifugation. Based on the standard curves, the DOX content in the mice blood and various tissues was tested.

2.15. In vivo antitumor effect of *HLA4P@DOX*

We randomly divided the CT-26 bearing mice (19–25 g) into 4 groups ($n = 5$). The treatments were performed (this time point was recorded as "day 1") when the CT-26-bearing mice's tumor volume reached an average size ~70 mm^3. The CT-26-bearing mice groups were intravenously injected once. Free DOX (6 mg/kg), **HLA4P,** PBS, and **HLA4P@DOX** (6 mg/kg eq.) were i.v. injected into the mice, respectively. The tumor volume was determined by an electronic vernier caliper. The CT-26 tumor volume was analyzed by the formula: $V = e^2 \times E/2$, where E and e were the longest and shortest diameter of the CT-26 tumor, respectively. The CT-26 mice were weighed every two days, and then the survival rate of mice was tested all the time.

2.16. Histological analysis

Major organs were obtained from ICR mice or CT-26 tumor-bearing mice. Tumors and major organs were obtained from CT-26 tumor-bearing mice and fixed with EDTA/formalin solution. After embedded, H&E was used to stain the various tissue samples.

2.17. Ethics statement

All animal experimental protocols were approved by the Animal Care and Use Committee of Wuhan University.

2.18. Statistical analysis

All statistical data was analyzed by GraphPad Prism 8.0.1 (GraphPad Software Inc). One-way ANOVA was employed for multiple comparisons. $^*P < 0.05$, $^{**}P < 0.01$, $^{***}P < 0.001$ and $^{****}P < 0.0001$ were considered as statistically significant results.

3. Results and discussion

3.1. Rational design and synthesis

Four new type small-molecule NIR-II fluorophores **HLAn** ($n = 1$–4) were designed. Thiophene or dodecyl-thiophene was the first donor (D1), and substituted triphenylamine or benzene was employed as the second donor (D2). Density function theory (DFT) was firstly used to investigate the electronic properties of **HLAn** (n = 1–4) by employing the B3LYP/6-31G(d) method with Gaussian 09 software. As is clearly seen in Fig. 2a, the highest occupied molecular orbitals (HOMOs) of **HLAn** (n = 1–4) are mainly delocalized on the whole backbone. The HOMOs of **HLA1** and **HLA2** are much higher than those of **HLA3** and **HLA4**. The lowest unoccupied molecular orbitals (LUMOs) are mainly localized on the electron acceptor TTD. The optical bandgaps of **HLA1**, **HLA2**, **HLA3,** and **HLA4** are 1.63 ev, 1.77 eV, 1.48 eV, and 1.57 eV, respectively (Fig. 2a), which are close to the optical bandgap of **CH1055** (1.5 eV), a critical value for BBTD-based NIR-II fluorophores. For the ground-state (S_0) and first singlet excited state ($S_{1)}$ geometries at optimized state, the included angles between TTD and D1, and between D1 and D2, gradually enlarge with the increase of the steric hindrance of side chains on D1 (Fig. 2b).

HLAn ($n = 1$–4) was efficiently prepared as outlined in Fig. 2c. Briefly, the key intermediates 4,6-bis(5-bromo-2-thienyl)thieno[3,4-c][1,2,5] **3** and 4,6-bis(5-bromo-3-dodecyl-2-thienyl)thieno **4** were obtained through Zn powder reduction, *N*-thionylaniline-induced reaction, and Stille coupling from commercial available 2,5-dibromo-3,4-dinitrothiophene. Subsequently, Suzuki coupling reaction of **3–4** and **5**, **3–4** and **6** resulted in the formation of **HLAn** ($n = 1$–4) with overall yields of ~30%. The corresponding chemical structures were well characterized and confirmed by ^{1}H NMR, ^{13}C NMR, and MOLDI-TOF-MS. Finally, **HLAnP** (n = 1–4) conjugate was synthesized by the coupling reaction of PEG_{2K}-NH_2 and PEG_{2K}-alkynyl, which self-assembled into micelles (Fig. 2d). Successful synthesis of **HLAnP** (n = 1–4) conjugate was also confirmed by ^{1}H NMR and MOLDI-TOF-MS. Details of the synthesis process and characterizations are shown in Fig. S1–S40.

3.2. Photophysical and self-assembly properties of TTD-based fluorophores

We examined the optical properties of TTD-based fluorophores *in vitro* under different conditions (Supplementary Table 1). Normalized

UV–vis spectra in Fig. 3a showed that **HLAn** (n = 1–4) possessed a significant absorption profile in the NIR-I range with a maximum at 678–726 nm (ε = 4.3–6.0 × 10^3 mol^{-1}·cm^{-1}), and presented notably high NIR-II fluorescence emission peaks at 967–1034 nm (Fig. 3b). The fluorescence QYs of **HLAn** (n = 1–4) were 4.3–6.0% under 785 nm excitation in dichloromethane ($QY_{IR\text{-}26}$ = 0.5%, Fig. S41). **HLAnP** (n = 1–4) exhibited a broad peak with reduced extinction coefficient in aqueous solution, resulting in bathochromic shift (1012–1069 nm, QYs = 0.15%–1.3%, Fig. 3d, Supplementary Table 1). The alkyl chains on the thiophene rings enhanced the QYs (QY_{HLA2P} = 1.3%, QY_{HLA4P} = 1.1%). Then, the photo-stability of **HLAnP** (n = 1–4) was investigated in phosphate-buffered saline (PBS) (Fig. 3e). After exposure to laser excitation for 60 min (808 nm, 100 mW/cm^2), no obvious photo-bleaching of **HLAnP** (n = 1–4) solution was observed. In sharp contrast, under the same conditions, ICG was dramatically decomposed. **HLAnP** (n = 1–4) solution was very stable even at room temperature over 7 days (Fig. S43). As illustrated in Fig. S42, the NIR-II fluorescence signals of **HLA4P** were much higher than others at different LP filters.

The shape, size, and surface chemical potential of fluorophore nanoparticles have a strong influence on their pharmacokinetics, passive tumor targeting, and excretion [58]. Thus, the self-assembly behavior and zeta potential of **HLAnP** (n = 1–4) in aqueous solution were investigated to understand their clearance pathways and tumor targeting mechanisms. The critical micelle concentrations (CACs) of **HLAnP** (n = 1–4) in aqueous solutions were determined to be 32 μM, 17 μM, 19 μM, and 54 μM, respectively (Fig. S44). It is known that **HLA2P** and **HLA4P** can form stable micelles very easily in aqueous solution due to their longer hydrophobic tails. They may have similar free energies of

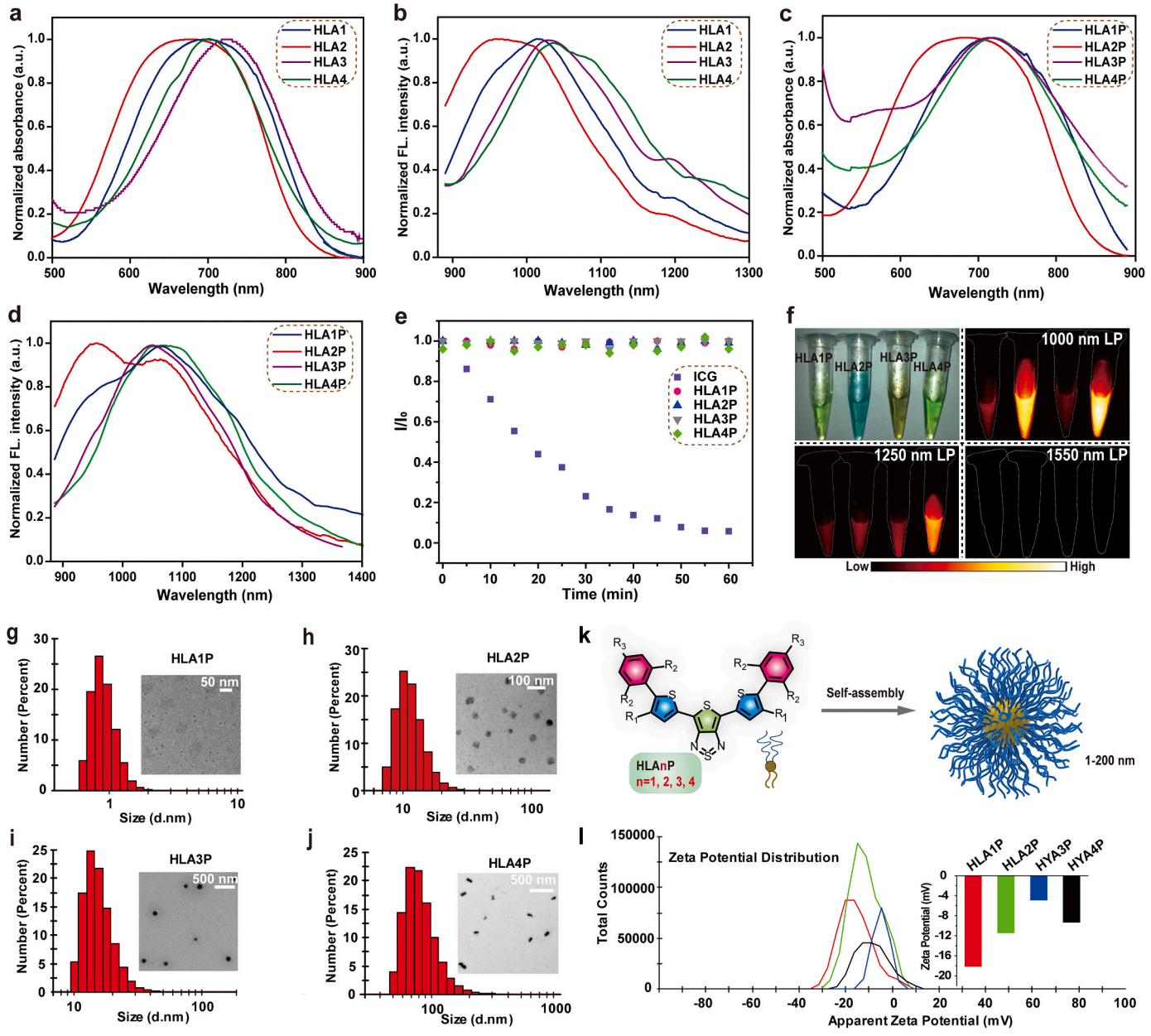

Fig. 3. Optical and self-assembled properties of **HLAn** and **HLAnP** (n = 1–4). (a) Absorption spectra and (b) emission spectra of **HLAn** (n = 1–4) in DCM. (c) Absorption spectra and (d) fluorescent emission spectra of **HLA1–4** in aqueous solution. (e) Photo-stabilities of **HLA4P** in PBS compared to ICG in PBS. (f) NIR-II fluorescent imaging of **HLA1P–4P** in water at the identical OD with various LP filters (1000, 1250 and 1550 nm). TEM, DLS, and zeta potential data of **HLA1P–4P** in aqueous solution. TEM images and DLS data of **HLA1P** (g), **HLA2P** (h), **HLA3P** (i) and **HLA4P** (j). (k) Schematic illustration of the self-assembly progress of **HLA1P–4P**. (l) Zeta potential data of **HLA1P–4P**.

micellization [58]. Dynamic light scattering (DLS) was employed to test the hydrodynamic radius of 1–200 nm of **HLAnP** (n = 1–4), consistent with the enhanced micellar size observed from transmission electron microscope (TEM) images (Fig. 3g-j). The introduction of dodecyl groups on the thiophenes enlarged their hydrophobic parts, which is probably conduced to the increase of self-assembly sizes (**HLA2P** *vs* **HLA1P** and **HLA4P** *vs* **HLA3P**). The **HLAnP** (n = 1–4) micelles exhibited negative surface charges as confirmed by their zeta-potentials (Fig. 3l).

3.3. *The in vivo pharmacokinetics and biocompatibility of **HLAnP** (n = 1–4)*

PEG, a stealth material, can resist nonspecific protein absorption, and increase *in vivo* circulation time [59]. However, multiple chemotherapeutic administration of PEGylated molecules or nanocarriers would cause accelerated blood clearance (ABC), which would severely affect drug bioavailability and targeting ability [60]. The ABC phenomenon may be attributed to the interaction of the hydrophobic character of PEG and highly immunogenic proteins, generating anti-PEG antibodies [60]. The blood half-life ($t_{1/2}$) of **HLAnP** (n = 1–4) was first evaluated after repeated injections, and showed the following ranking: **HLA4P** (70 h) > **HLA3P** (18 h) > **HLA2P** (8.2 h) > **HLA1P** (0.5 h) (Fig. 4a–b). NIR-II vascular imaging further confirmed the prolonged blood persistence of **HLA4P** (Fig. S45). Then the immune responses of **HLAnP** (n = 1–4) were investigated by measuring the serum immunoglobulin M (IgM) level at the fifth day post the first intravenous injection, and the serum immunoglobulin G (IgG) level at the fifth day post the second intravenous injection (Fig. 4c–d). The results indicated that **HLAnP** (n = 1–4) induced negligible immune responses. The K_d values of **HLAnP** (n = 1–4) with the albumin (the most abundant protein in

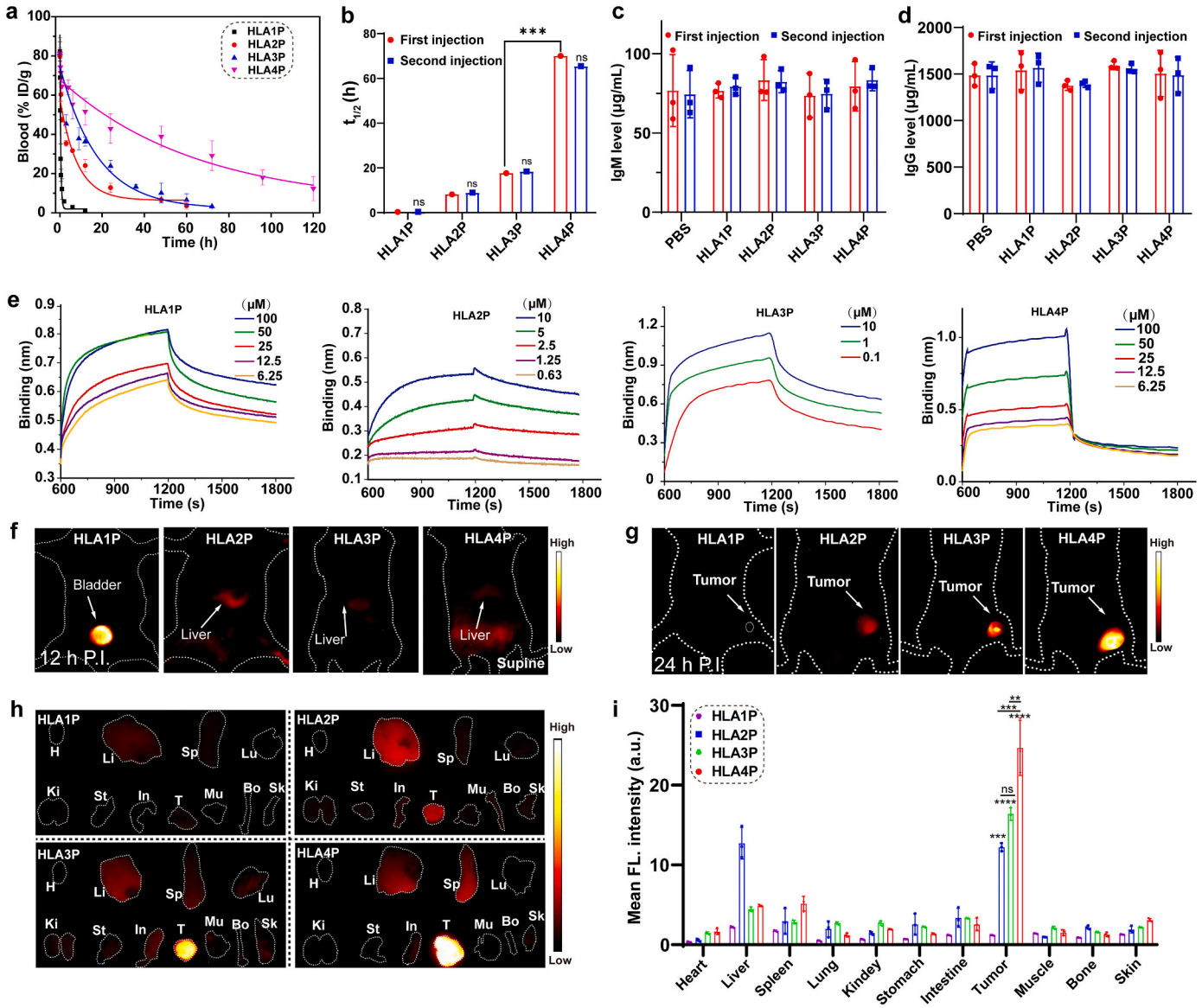

Fig. 4. *In vivo* pharmacokinetics and biocompatibility of **HLA1P–4P**. (a) The blood half-life circulation curve of **HLA1P–4P** measured by fitting the data from the average fluorescence intensity of blood samples post-injection (b) The half-life of **HLA1P–4P** in blood after the first i.v. injection and second i.v. injection. (c) IgM levels on the fifth day after the first i.v. injection of **HLA1P–4P**. (d) IgG levels on the fifth day after the second i.v. injection of **HLA1P–4P.** (e) Kinetic binding assay of **HLA1P–4P** to albumin was tested by biolayer interferometry. (f) NIR-II fluorescence images of ICR mice in supine position at 1 h post injection of **HLA1P–4P** (1000 nm LP, 50 ms). (g) *In vivo* tumor imaging at 24 post injection of **HLA1P–4P (**0.2 mL, 200 μM) in 4 T1 mice (n = 3). (h) *Ex vivo* bio-distribution of **HLA1P–4P** at 48 h post injection into 4 T1 mice evaluated through NIR-II fluorescence imaging (20 ms, 808 nm laser, 92 mW/cm^2). (i) Mean fluorescence intensity of histological distribution of 4 T1 mice (n = 3) at 48 h post injection of **HLA1P–4P**. All data are represented as the mean ± SD. **** $p < 0.0001$, *** $p < 0.001$, ** $p < 0.01$, and ns not significant.

blood) were estimated to be 241 nM, 312 nM, 109 nM, and 422 nM, respectively (Fig. 4e). In addition, a 3-(4,5-dimethyl-2-thiazolyl)-2,5-diphenyl-2-*H*-tetrazolium bromide (MTT) assay was employed to explore the cellular toxicity of **HLAnP** (n = 1–4) on 4 T1 mouse breast cancer cells and L02 human liver cells. No obvious cytotoxicity was observed at concentrations up to 50 μM (Fig. S46). We further tested the safety profile of **HLA4P** administered to mice. After **HLA4P** (200 μL, 200 μM) was administered to ICR mice (n = 3) through intravenous injection (i.v.) to estimate short-term and long-term physiological toxicity, there were no abnormally increased levels of typical biochemical blood biomarkers associated with liver and kidney functions such as total bilirubin (TBIL), serum creatinine (CREA), blood urea nitrogen (BUN), aspartate aminotransferase (AST), alanine aminotransferase (ALT), or alkaline phosphatase (ALP) in **HLA4P**-treated animals at 1, 7, or 21 days p.i. of **HLA4P** compared to the PBS group (Fig. S47–S49). In addition, the heart, spleen, liver, kidney, and lung of **HLA4P** groups had no significant lesions. Thus, the minimal cytotoxicity, the long-term and short-term physiological toxicity demonstrates

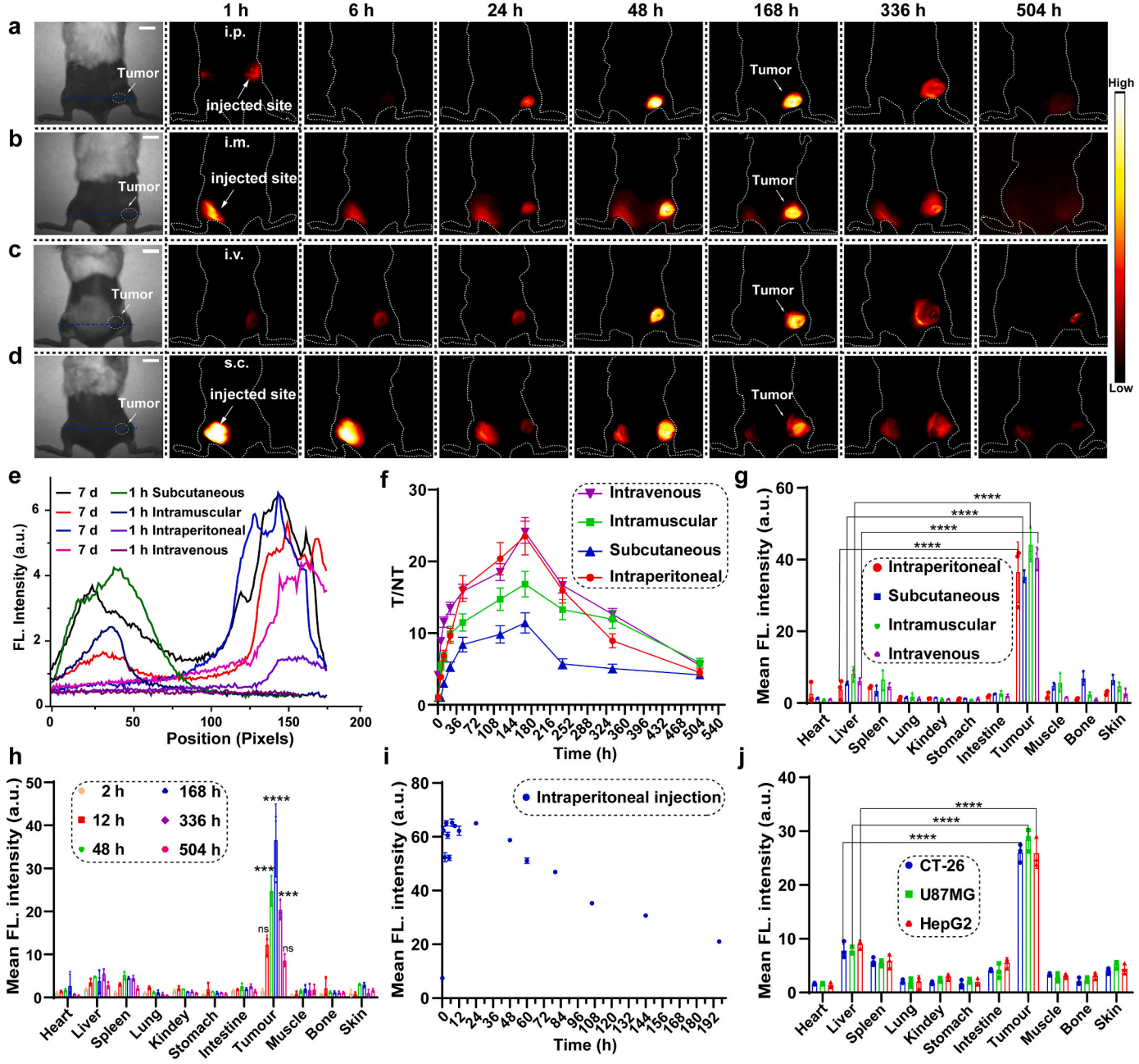

Fig. 5. Various injection modes for NIR-II fluorescent tumor imaging with **HLA4P**. (a) Representative non-invasive NIR-II fluorescent imaging of 4 T1 tumor imaging in 4 T1 BALB/c mice i.p. injected with **HLA4P** (200 μL, 200 μM) (n = 4), (b) Intramuscular injected (n = 4), (c) Tail vein injected (n = 4), (d) Subcutaneous injected (n = 4). (e) The fluorescent intensity profiles indicated by blue dotted lines labeled in a, b, c, and d. (f) The T/NT of four different injection sites at different time points. (g) Bio-distribution in 4 T1 mice (n = 3) after 168 h *via* four different injection routes (**HLA4P**, 200 μL, 200 μM), (1000 nm LP filter, 10 ms exposure time, 808 nm laser excitation, 100 mW/cm^2). (h) Bio-distribution of 4 T1 mice (n = 3) at various time points (2 h–504 h) after i.p. injection of **HLA4P** (200 μL, 200 μM). (i) The half-life in blood of **HLA4P** tested by fitting the resulting data from the average fluorescent intensity of mice's blood samples at various time points after i.p. injection. (j) Bio-distribution in CT-26, HepG2, and U87MG mice (n = 3) at 168 h after i.p. injection of **HLA4P** (200 μL, 200 μM). All data are represented as the mean ± SD. **** $p < 0.0001$, *** $p < 0.001$, ** $p < 0.01$, and ns not significant. (For interpretation of the references to colour in this figure legend, the reader is referred to the web version of this article.)

that **HLA4P**, as a novel NIR-II organic fluorophore, has good biocompatibility and potential anti-cancer applications.

To study the excretion pathway, **HLAnP** (n = 1–4, 200 μL, 200 μM) were i.v. injected into ICR mice. The strong fluorescence intensity in bladder and urine from **HLA1P**-treated mice (n = 3) indicated the renal clearance pathway of **HLA1P** (Fig. 4f, Fig. S50 and Fig. S51). In contrast, the predominance of NIR-II signals in liver and feces suggested that **HLA4P** was mainly excreted through the hepatobiliary clearance pathway (Fig. 4f, Fig. S52).

3.4. NIR-II tumor imaging of *HLAnP* (n = 1–4)

We then examined the *in vivo* NIR-II imaging performance of **HLAnP** (n = 1–4) in 4 T1 xenograft tumor-bearing BALB/c mice (n = 3 per group). **HLAnP** (n = 1–4) were intravenously injected into BALB/c mice bearing 4 T1 xenografts at a dose of 200 μM. **HLA1P** barely accumulated around the tumor region, and no obvious NIR-II fluorescence signals were detected after 6 h, since they were eliminated quickly from the blood circulation (Fig. 4g). 4 T1 tumors were significantly distinguished from the surrounding background tissues for **HLA2P**, **HLA3P**, and **HLA4P** *via* the EPR effect after 6 h post-injection, and the fluorescent intensity order of 4 T1 tumors was **HLA4P** > **HLA3P** > **HLA2P** (Fig. 4g, 1000 LP, 20 ms). Then *ex vivo* fluorescence imaging was conducted to examine the biodistribution profile after 48 h post-injection (Fig. 4h). Besides tumor sites, **HLAnP** (n = 2–4) were mainly distributed in the liver, consistent with *in vivo* NIR-II imaging (Fig. 4g). The mean fluorescent intensity of probes distribution in 4 T1 mice (n = 3) at 48 h post-injection was in the following order: **HLA4P** > **HLA3P** > **HLA2P** (Fig. 4i, 1000 LP, 20 ms). **HLA4P** exhibited striking accumulation in 4 T1 tumors owing to ultralong blood circulation, low binding affinity, as well as robust EPR effect. Thus, in view of its remarkable optical properties and unique tumor imaging performance, **HLA4P** was selected for further *in vivo* study.

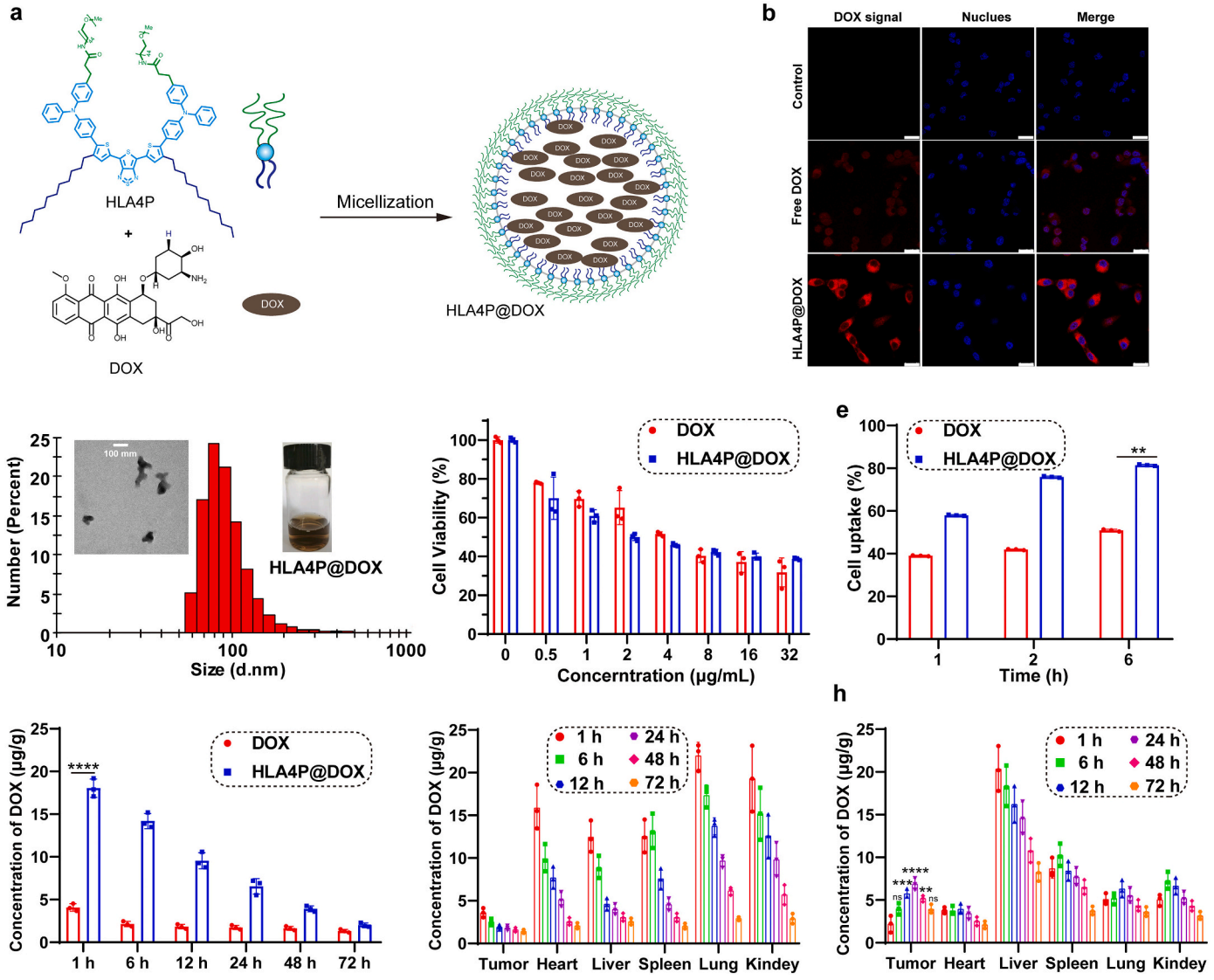

Fig. 6. Cellular uptake and biodistribution of **HLA4P@DOX**. (a) Schematic illustration of the preparation of **HLA4P@DOX** by self-assembly. (b) After treatment with free DOX (C_{DOX} = 60 μM) and **HLA4P@DOX** (C_{DOX} = 60 μM) at 8 h in CT-26 cells, cell uptake was imaged by a confocal microscope. (Scale bar = 25 μm). (c) The DLS and TEM of **HLA4P@DOX**. (d) The cell viability of drug-resistant CT-26 cells with **HLA4P@DOX** and DOX measured by MTT assay. (e) Cellular uptake was measured by a flow cytometry with free DOX (C_{DOX} = 60 μM) and **HLA4P@DOX** (C_{DOX} = 60 μM) at 1 h, 2 h and 6 h in CT-26 cells. (f) Concentrations of **HLA4P@DOX** and free DOX in the blood at different time points post i.v. injection, biodistribution of free DOX (g) and **HLA4P@DOX** (h) in various organs of CT-26 mice at different time points post injection (n = 3). All data are represented as the mean ± SD. **** $p < 0.0001$, *** $p < 0.001$, ** $p < 0.01$, and ns not significant.

3.5. NIR-II imaging with different injection routes

To investigate the feasibility of multiple administration routes for biological applications, **HLA4P** was administered to BALB/c mice bearing 4 T1 xenografts *via* i.v., intraperitoneal injection (i.p.), intramuscular injection (i.m.), or subcutaneous injection (s.c.). As shown in Fig. 5a–d, the subcutaneous transplantation tumor model of 4 T1 cancer was established on the right side of mice. **HLA4P** (200 μL, 200 μM) was i.p. administered to 4 T1 tumor-bearing mice ($n = 4$) (Fig. 5a). Interestingly, the outline and peristalsis of the intestine could be clearly visualized, and the fluorescence signals in the abdomen gradually diminished at 6 h post i.p. (Fig. S53). Meanwhile, NIR-II fluorescence signals of hindlimb vessels were notably identified, suggesting that **HLA4P** was absorbed into the blood circulation. The tumor to normal tissue (T/NT) signal ratio gradually increased over times (1 h, 2 h, 12 h, 48 h and 7 *D*), and reached a maximum at ~25 at 7 days post i.p. (Fig. 5f). Then, **HLA4P** (200 μL, 200 μM) was injected into 4 T1 tumor-bearing mice *via* the left hind leg muscle, left back, and tail vein by i.m., s.c. or i.v. routes, respectively. Injection site's fluorescence signals were initially very strong, and then gradually decreased (Fig. 5b–d). The T/NT signal ratio gradually increased, and reached a maximum at ~12, ~ 19, and ~ 25 at 7 days post-injection, respectively (Fig. 5a–5f). Furthermore, *ex vivo* bio-distribution of **HLA4P** was investigated at 7 D post-injection with different injection routes, and the quantitative analysis of the NIR-II fluorescent intensities of heart, liver, lung, spleen, kidney, intestine, stomach, tumor, bone, muscle, and skin tissues were evaluated (1000 nm, 10 ms exposure time, 100 mW/cm^2) (Fig. 5g–h). The NIR-II fluorescence intensity of 4 T1 tumors were significantly higher than those of other tissues (Fig. S54). As shown in Fig. 6g, the tumor-to-liver signal ratio (T/L) of mice after i.p, i.m, s.c. or i.v. of **HLA4P** was 6.7, 6.7, 4.9 and 6.4 respectively. All these results further support the excellent tumor accumulation of **HLA4P**.

The blood half-life of **HLA4P** with different injection routes was also explored (Fig. 5i and Fig. S55). **HLA4P** (200 μL, 200 μM) was injected into ICR mice by i.p, s.c. or i.m. routes, respectively. The blood fluorescence signal gradually increased shortly after injection. Compared with i.m. and s.c. routes, **HLA4P** was absorbed faster by the i.p. method *via* the abundant blood vessels in the peritoneum of the abdominal cavity. The absorption and clearance of **HLA4P** in blood countered balance at 24 h, 13 h and 30 h post i.p, post i.m or post s.c. routes, respectively.

In addition, the NIR-II imaging performance against various tumors was studied after i.p. injection. **HLA4P** (200 μL, 200 μM) was i.p. injected into U87MG-bearing nude mice, CT26-bearing BALB/c mice, and HepG2-bearing nude mice. The whole process was monitored under 808 nm laser irradiation (10 ms exposure time, 100 mW/cm^2) using 1000 nm LP. All tumors gradually illuminated were notably identifiable at 12 h, and achieved the highest intensity at 168 h post injection (Fig. S56). Subsequently, these mice were sacrificed. The NIR-II fluorescence intensities of U87MG, HepG2, and CT26 tumors were much stronger than those of heart, spleen, liver, kidney, lung, intestine, stomach, muscle, bone, or skin tissue (1000 nm, 10 ms exposure, 100 mW/cm^2) (Fig. 5j). The tumor tissue imaging was characterized by NIR-II fluorescence imaging (50 ms, 1000 nm, 808 nm laser excitation). The fluorescent intensity **HLA4P** in the longitudinal section of the cross section of 4 T1 tumor and CT-26 tumor was shown in Fig. S57. These promising results indicate that self-assembling **HLA4P** could be utilized for various tumors and administration routes.

3.6. The construction and characterization of *HLA4P@DOX*

To explore the drug loading content and controlled release capabilities of **HLA4P**, doxorubicin (DOX), an anti-cancer medicine, was used to serve as a model medicine. **HLA4P@DOX** was prepared through typical nano-encapsulation methods (Fig. 6a). UV–vis spectra in Fig. S58 showed that HLA4P@DOX possessed a significant absorption profile at 450–900 nm, and presented fluorescence emission peaks at ~590 nm and 1035 nm. **HLA4P@DOX** was characterized by TEM and DLS, with average sizes of ~150 nm and ~ 246 nm, respectively (Fig. 6c), slightly higher than the self-assembly sizes of individual **HLA4P**. The zeta potential of **HLA4P@DOX** in water was 2.89 eV (Fig. S59). The encapsulation efficiency of **HLA4P@DOX** was measured as ~65% based on UV–vis absorbance of DOX (Fig. S60). To explore the pharmacological activity of **HLA4P@DOX**, the cytotoxicity against CT-26 cells was determined by MTT assay. As exhibited in Fig. 6d, dose-dependent cytotoxicity was observed for **HLA4P@DOX** and DOX. The IC_{50} values of **HLA4P@DOX** and DOX were 3.82 μg/mL and 5.32 μg/mL, respectively. In addition, no obvious cellular toxicity to normal liver cells (L02) was observed after exposure to 50 μM of **HLA4P@DOX** and **HLA4P** for 24 h (Fig. S61). These results demonstrate that this fluorescent drug delivery platform has no obvious cytotoxicity, which is vital for the application in NIR-II imaging and image-guided therapy.

To verify the cell uptake of DOX and **HLA4P@DOX**, the flow cytometry analysis was conducted on CT-26 cells. When CT26 cells were cultured with free DOX for 6 h, the drug uptake efficiency was ~50%. In comparison, the drug uptake was increased to ~80% after incubation for 6 h with **HLA4P@DOX** (Fig. 6e and Fig. S62), which indicated that **HLA4P@DOX** promoted DOX's cell internalization and accumulation. The improved cellular uptake of **HLA4P@DOX** in CT-26 cells was further demonstrated by confocal laser scanning microscopy (Fig. 6b). The red fluorescence of **HLA4P@DOX** was much stronger than that of free DOX, demonstrating much higher uptake in CT-26 cells (Fig. 6b). The improved DOX biodistribution of **HLA4P@DOX** in CT-26 mice model were estimated (Fig. 6f–6h). The biodistribution of DOX in various organs and tumors were also analyzed. Notably, the concentration of DOX in mice' blood for **HLA4P@DOX** was 4.5-fold higher than that of free DOX at the identical time point, indicating that **HLA4P** as a novel DOX carrier markedly prolongs the circulation time of DOX in the mice' blood. Furthermore, the concentrations of free DOX in tumor achieved the maximum (2.93 μg/g tissue) at 1 h post-injection, and then decreased until the end of the experiment (Fig. 6g–6h). For **HLA4P@DOX**, the content of DOX in tumor increased from 1 h to 24 h, and achieved its maximum (6.87 μg/g tissue) at 8 h post-injection. Our results suggest that **HLA4P@DOX** achieves an enhanced DOX content at the tumor site than free DOX, owing to EPR effect in solid tumors. Furthermore, the concentration of DOX in the heart for free DOX (17.4 μg/g tissue) at 1 h post-injection was ~5.4-fold higher than that of **HLA4P@DOX** (3.2 μg/g tissue). These results indicate that **HLA4P@DOX** can minimize the highly problematic cardiotoxicity of free DOX.

3.7. *HLA4P@DOX* for real-time NIR-II fluorescence imaging and image-guided therapy

The anti-tumor capability of **HLA4P@DOX** was further confirmed by the CT-26 tumor-bearing models. CT-26 cells were injected into the subcutaneous site of BALB/c mice. When the tumor size reached ~70 mm^3, treatments were conducted by i.v. of PBS buffer, free DOX (6 mg/kg), **HLA4P** (6 mg/kg), or **HLA4P@DOX** (6 mg/kg DOX). The tumor size and body weight were measured every 2 days. The growth rate of CT-26 tumors treated with PBS and **HLA4P** was very rapid, and after 14 days' treatment the tumor volumes in the two control groups had increased ~13-fold and ~ 12-fold (Fig. 7b). However, the growth rate of CT-26 tumors treated with free DOX slowed down in the initial 6 days post injection. The average tumor volume in the free DOX-treated group increased 6-fold after 14 days treatment. **HLA4P@DOX** effectively limited tumor growth, and restricted the mean tumor size to a ~ 3.5-fold increase after 14 days treatment (Fig. 7d). Moreover, the tumor size kept nearly constant during the initial 8 days after injection. *Ex vivo* tumor weight on day 14 further confirmed the best therapeutic effect of **HLA4P@DOX** among all groups (Fig. 7c). More importantly, the entire treatment process was precisely monitored by NIR-II fluorescence imaging. A remarkable NIR-II signal was achieved at the tumor site with

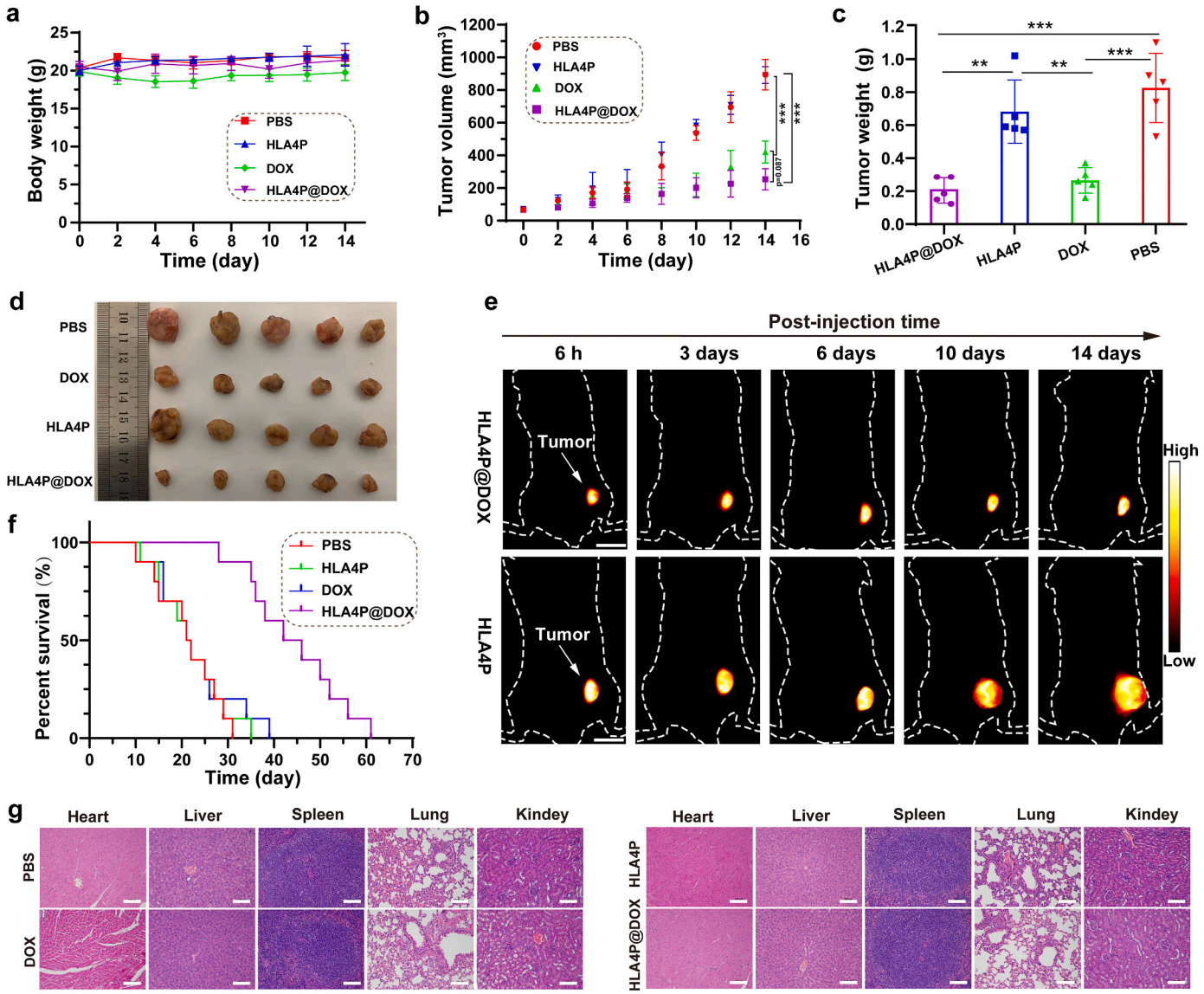

Fig. 7. *In vivo* therapeutic evaluation of **HLA4P@DOX**. (a) Animal body weight changes in PBS, DOX, **HLA4P**, and **HLA4P@DOX** groups. (b) Intravital tumor growth curves of CT-26 mice with various treatments (n = 10). (c) Weight statistics of tumor *ex vivo* (n = 5). (d) Images of CT-26 tumors *ex vivo* at day 14 from mice given various treatments. (e) Intravital NIR-II fluorescent imaging of **HLA4P** and **HLA4P@DOX** groups, exposure time: 6 h (70 ms), 3 days (20 ms), 6 days (20 ms),10 days (30 ms) and 14 days (50 ms). (f) Kaplan-Meier curves exhibiting survival of CT-26 mice in distinct groups. (g) H&E staining of primary organs obtained at day 14. Scale bar: 100 mm. All data are represented as the mean ± SD. *** $p < 0.001$, ** $p < 0.01$, and ns not significant.

high T/TN (> 25), and persisted for more than 14 days, suggesting the superior tumor-targeting ability and the ultralong tumor retention of **HLA4P@DOX** (Fig. 7e). These findings were quite accord with previous results for *in vivo* tumor imaging.

The body weight of CT-26 mice in the free DOX group showed a slight diminution in the first 6 days after treatment owing to the notable side effects of DOX. Conversely, **HLA4P@DOX** allowed a moderate growth in CT-26 mice body weight (Fig. 7a). In addition, the systemic toxicity of **HLA4P@DOX** in CT-26 mice ($n = 5$) was investigated using H&E staining. The arrangement of the myocardial fibers in horizontal and vertical lines appeared disordered after treatment with free DOX (Fig. 7g). In sharp contrast, the hearts of CT-26 mice treated with **HLA4P@DOX** exhibited distinct and well-dispersed cardiomyocytes, suggesting the toxicity of DOX had been decreased. Pathological changes in other organs were barely observed. Fig. 7f exhibits the survival curves of CT-26 mice in each group ($n = 10$). All the CT-26 mice in PBS and **HLA4P** groups died during the 35 days after injection owing to the markedly fast growth of CT-26 tumor. In the free DOX treated group, only 2 of 10 mice survived for 33 days. Conversely, in the **HLA4P@DOX** group, half of the CT-26 mice survived for 35 days, although 9 of 10 died after 60 days. Together, these results suggested that **HLA4P@DOX** can be used for accurate tumor diagnosis and real-time image-guided therapy.

4. Conclusion

In summary, we have engineered next-generation D-A-D type NIR-II fluorescence molecules **HLAn** (n = 1–4) based on a new acceptor core TTD. After PEGylation, **HLAn** (n = 1–4) exhibited great amphiphilicity, and ability to self-assemble into micelle-like nanoparticles in aqueous solution. Optical and pharmacokinetic studies demonstrated that the QYs (0.15–1.3%) and blood circulation time ($t_{1/2}$ = 0.5–70 h) of such bright fluorophores were remarkably enhanced by introducing long aliphatic chains at the ortho-position of the thiophene ring (adjacent to donor). Among them, **HLA4P** possessed long blood circulation time (70 h), exceptional nonfouling performance, minimal immunogenicity, and

was mainly excreted *via* the hepatobiliary system. Notably, **HLA4P** achieved various tumor-bearing imaging (4 T1, CT26, U87MG and HepG2) in the NIR-II window with minimal background interference, and minimal RES uptake after intravenous, intraperitoneal, intramuscular, or subcutaneous injection. The nonfouling performance of **HLA4P** enabled high T/TN (> 25) and prolonged tumor retention time (> 21 days). More importantly, the long blood circulation time and amphiphilic structure render **HLA4P** an ideal fluorescent nanoplatform for drug delivery. A novel theranostic drug **HLA4P@DOX** was successfully prepared with ~65% DOX encapsulation efficiency. Its sustained DOX release behavior, enhanced therapeutic effect, and low toxicity of **HLA4P@DOX** were investigated *in vivo*. Remarkably, the process of tumor treatment could be dynamically monitored under the guidance of real-time NIR-II fluorescence imaging in an extended time window (> 14 days) owing to the prolonged tumor retention time of **HLA4P**. In addition, the imaging effect using **HLA4P** *via* intraperitoneal administration is superior to the conventional intravenous administration because of its low technical requirements and accurate injection dose. Therefore, these results collectively suggested the feasibility of **HLA4P** as a long-persisting NIR-II nanoprobe for drug delivery and image-guided cancer therapy. We expect that our study will provide a new perception on the design of novel trackable drug delivery systems based on small-molecule NIR-II fluorophores.

Declaration of Competing Interest

The authors declare no competing financial interest.

Acknowledgments

This work was partially supported by grants from the National Key R&D Program of China (2020YFA0908800), NSFC (82111530209, 81773674, 91959103, 81573383, 21763002), Shenzhen Science and Technology Research Grant (JCYJ20190808152019182), the Applied Basic Research Program of Wuhan Municipal Bureau of Science and Technology (2019020701011429), Hubei Province Scientific and Technical Innovation Key Project (2020BAB058), the Local Development Funds of Science and Technology Department of Tibet (XZ202102YD0033C, XZ202001YD0028C), and the Fundamental Research Funds for the Central Universities.

Appendix A. Supplementary data

Supplementary data to this article can be found online at https://doi.org/10.1016/j.jconrel.2022.01.005.

References

[1] H. Sung, J. Ferlay, R.L. Siegel, M. Laversanne, I. Soerjomataram, A. Jemal, F. Bray, Global Cancer Statistics, GLOBOCAN estimates of incidence and mortality worldwide for 36 cancers in 185 countries, CA Cancer J. Clin. 71 (2021) (2020) 209–249.

[2] S. Chen, Y. Zhong, W. Fan, J. Xiang, G. Wang, Q. Zhou, J. Wang, Y. Geng, R. Sun, Z. Zhang, Y. Piao, J. Wang, J. Zhuo, H. Cong, H. Jiang, J. Ling, Z. Li, D. Yang, X. Yao, X. Xu, Z. Zhou, J. Tang, Y. Shen, Enhanced tumour penetration and prolonged circulation in blood of polyzwitterion–drug conjugates with cell-membrane affinity, Nat. Biomed. Eng. (2021), https://doi.org/10.1038/s41551-021-00701–4.

[3] J. Zhou, L. Rao, G. Yu, T.R. Cook, X. Chen, F. Huang, Supramolecular cancer nanotheranostics, Chem. Soc. Rev. 50 (2021) 2839–2891.

[4] Y. Zhang, S. Ma, X. Liu, Y. Xu, J. Zhao, X. Si, H. Li, Z. Huang, Z. Wang, Z. Tang, W. Song, X. Chen, Supramolecular assembled programmable nanomedicine as in situ cancer vaccine for cancer immunotherapy, Adv. Mater. 33 (2021) 2007293.

[5] Y. Wang, C. Xu, M. Meng, L. Lin, Y. Hu, K. Hao, S. Sheng, S. Zhang, J. Wu, F. Liu, X. Jiang, H. Tian, X. Chen, Precise regulation of inflammation and immunosuppressive microenvironment for amplified photothermal/immunotherapy against tumour recurrence and metastasis, Nano Today 40 (2021), 101266.

[6] D. Zhong, D. Zhang, T. Xie, M. Zhou, Biodegradable microalgae-based carriers for targeted delivery and imaging-guided therapy toward lung metastasis of breast cancer, Small 16 (2020) 2000819.

[7] M. Ge, D. Xu, Z. Chen, C. Wei, Y. Zhang, C. Yang, Y. Chen, H. Lin, J. Shi, Magnetostrictive-piezoelectric-triggered nanocatalytic tumor therapy, Nano Lett. 21 (2021) 6764–6772.

[8] N. Panwar, A.M. Soehartono, K.K. Chan, S. Zeng, G. Xu, J. Qu, P. Coquet, K. Yong, X. Chen, Nanocarbons for biology and medicine: sensing, imaging, and drug delivery, Chem. Rev. 119 (2019) 9559–9656.

[9] X. Dong, A. Yang, Y. Bai, D. Kong, F. Lv, Dual fluorescence imaging-guided programmed delivery of doxorubicin and CpG nanoparticles to modulate tumor microenvironment for effective chemo-immunotherapy, Biomaterials 230 (2020), 119659.

[10] Y. Cao, J. Yang, D. Eichin, F. Zhao, D. Qi, L. Kahari, C. Jia, M. Peurla, J. M. Rosenholm, Z. Zhao, S. Jalkanen, J. Li, Self-synthesizing nanorods from dynamic combinatorial libraries against drug resistant cancer, Angew. Chem. Int. Ed. 60 (2021) 3062–3070.

[11] C. Song, Y. Li, T. Li, Y. Yang, Z. Huang, J.M. de la Fuente, J. Ni, D. Cui, Long-circulating drug-dye-based micelles with ultrahigh pH-sensitivity for deep tumor penetration and superior chemo-photothermal therapy, Adv. Funct. Mater. 30 (2020) 1906309.

[12] D. Liu, C. Poon, K. Lu, C. He, W. Lin, Self-assembled nanoscale coordination polymers with trigger release properties for effective anticancer therapy, Nat. Commun. 5 (2014) 4182.

[13] Y. Dai, J. Guo, T. Wang, Y. Ju, A.J. Mitchell, T. Bonnard, J. Cui, J.J. Richardson, C. E. Hagemeyer, K. Alt, F. Caruso, Self-assembled nanoparticles from phenolic derivatives for cancer therapy, Adv. Healthcare Mater. 6 (2017) 1700467.

[14] C. Li, Y. Zhang, G. Chen, F. Hu, K. Zhao, Q, Wang, engineered multifunctional nanomedicine for simultaneous stereotactic chemotherapy and inhibited osteolysis in an orthotopic model of bone metastasis, Adv. Mater. 29 (2017) 1605754.

[15] W. Fan, B. Yung, P. Huang, X. Chen, Nanotechnology for multimodal synergistic cancer therapy, Chem. Rev. 117 (2017) 13566–13638.

[16] K.A. Carter, S. Shao, M.I. Hoopes, D. Luo, B. Ahsan, V.M. Grigoryants, W. Song, H. Huang, G. Zhang, R.K. Pandey, J. Geng, B.A. Pfeifer, C.P. Scholes, J. Ortega, M. Karttunen, J.F. Lovell, Porphyrin–phospholipid liposomes permeabilized by near-infrared light, Nat. Commun. 5 (2014) 3546.

[17] K. Fan, C. Cao, Y. Pan, D. Lu, D. Yang, J. Feng, L. Song, M. Liang, X. Yan, Magnetoferritin nanoparticles for targeting and visualizing tumour tissues, Nat. Nanotechnol. 7 (2012) 459–464.

[18] T. Nomoto, S. Fukushima, M. Kumagai, K. Machitani, Y. Arnida, M. Matsumoto, K. Oba, K. Miyata, N. Osada, K. Kataoka Nishiyama, Three-layered polyplex micelle as a multifunctional nanocarrier platform for light-induced systemic gene transfer, Nat. Commun. 5 (2014) 3545.

[19] K. Cai, X. He, Z. Song, Q. Yin, Y. Zhang, F.M. Uckun, C. Jiang, J. Cheng, Dimeric drug polymeric nanoparticles with exceptionally high drug loading and quantitative loading efficiency, J. Am. Chem. Soc. 137 (2015) 3458–3461.

[20] X. Hu, G. Liu, Y. Li, X. Wang, S. Liu, Cell-penetrating hyperbranched polyprodrug amphiphiles for synergistic reductive milieu-triggered drug release and enhanced magnetic resonance signals, J. Am. Chem. Soc. 137 (2015) 362–368.

[21] S. Senapati, A.K. Mahanta, S. Kumar, Controlled drug delivery vehicles for cancer treatment and their performance, Signal Transduct. Target. Ther. 3 (2018) 7–19.

[22] R.H. Fang, Y. Jiang, J.C. Fang, Cell membrane-derived nanomaterials for biomedical applications, Biomaterials 128 (2017) 69–83.

[23] X. Xu, H. An, D. Zhang, H. Tao, Y. Dou, X. Li, J. Huang, J. Zhang, A self-illuminating nanoparticle for inflammation imaging and cancer therapy, Sci. Adv. 5 (2019), t2953.

[24] Z. Cao, S. Jiang, Super-hydrophilic zwitterionic poly(carboxybetaine) and amphiphilic non-ionic poly(ethylene glycol) for stealth nanoparticles, Nano Today 7 (2012) 404–413.

[25] S. Yadav, A. Sharma, K. Kumar, Nanoscale self-assembly for therapeutic delivery, Front. Bioeng. Biotechnol. 8 (2020) 127.

[26] J.S. Suk, Q. Xu, N. Kim, J. Hanes, L.M. Ensign, PEGylation as a strategy for improving nanoparticle-based drug and gene delivery, Adv. Drug Deliv. Rev. 99 (2016) 28–51.

[27] M. Zhao, B. Li, P. Wang, L. Lu, Z. Zhang, L. Liu, S. Wang, D. Li, R. Wang, F. Zhang, Supramolecularly engineered NIR-II and upconversion nanoparticles in vivo assembly and disassembly to improve bioimaging, Adv. Mater. 30 (2018) 1804982.

[28] J. Mu, J. Lin, P. Huang, X. Chen, Development of endogenous enzyme-responsive nanomaterials for theranostics, Chem. Soc. Rev. 47 (2018) 5554–5573.

[29] F. Zhang, G. Zhu, O. Jacobson, Y. Liu, K. Chen, G. Yu, Q. Ni, J. Fan, Z. Yang, F. Xu, X. Fu, Z. Wang, Y. Ma, G. Niu, X. Zhao, X. Chen, Transformative nanomedicine of an amphiphilic camptothecin prodrug for long circulation and high tumor uptake in cancer therapy, ACS Nano 11 (2017) 8838–8848.

[30] X. Ji, L. Ge, C. Liu, Z. Tang, Y. Xiao, W. Chen, Z. Lei, W. Gao, S. Blake, D. De, B. Shi, X. Zeng, N. Kong, X. Zhang, W. Tao, Capturing functional two-dimensional nanosheets from sandwich-structure vermiculite for cancer theranostics, Nat. Commun. 12 (2021) 1124.

[31] D. Wei, Y. Yu, Y. Huang, Y. Jiang, Y. Zhao, Z. Nie, F. Wang, W. Ma, Z. Yu, Y. Huang, X. Zhang, Z. Liu, X. Zhang, H. Xiao, A near-infrared-II polymer with tandem fluorophores demonstrates superior biodegradability for simultaneous drug tracking and treatment efficacy feedback, ACS Nano 15 (2021) 5428–5438.

[32] J. Yang, X. Zhang, C. Liu, Z. Wang, L. Deng, C. Feng, W. Tao, X. Xu, W. Cui, Biologically modified nanoparticles as theranostic bionanomaterials, Prog. Mater. Sci. 118 (2021), 100768.

[33] G. Yu, B. Zhu, L. Shao, J. Zhou, M.L. Saha, B. Shi, Z. Zhang, T. Hong, S. Li, X. Chen, P.J. Stang, Host–guest complexation-mediated codelivery of anticancer drug and photosensitizer for cancer photochemotherapy, P. Nat. Acad. Sci. U. S. A. 116 (2019) 6618–6623.

[34] X. Liao, Y. Zheng, Z. Lin, Y. Shen, H. Lin, X. Liu, D. Zhang, B. Li, Self-assembled metallo-supramolecular nanoflowers for NIR/acidic-triggered multidrug release, long-term tumor retention and NIR-II fluorescence imaging-guided photo-chemotherapy, Chem. Eng. J. 400 (2020), 125882.
[35] C. Song, Y. Zhang, C. Li, G. Chen, X. Kang, Q. Wang, Enhanced nanodrug delivery to solid tumors based on a tumor vasculature-targeted strategy, Adv. Funct. Mater. 26 (2016) 4192–4200.
[36] Y. Men, S. Peng, P. Yang, Q. Jiang, Y. Zhang, B. Shen, P. Dong, Z. Pang, W. Yang, Biodegradable zwitterionic nanogels with long circulation for antitumor drug delivery, ACS Appl. Mater. Interfaces 10 (2018) 23509–23521.
[37] J.P.A. Ioannidis, B.Y.S. Kim, A. Trounson, How to design preclinical studies in nanomedicine and cell therapy to maximize the prospects of clinical translation, Nat. Biomed. Eng. 2 (2018) 797–809.
[38] H. Zhou, X. Zeng, A. Li, W. Zhou, L. Tang, W. Hu, Q. Fan, X. Meng, H. Deng, L. Duan, Y. Li, Z. Deng, X. Hong, Y. Xiao, Upconversion NIR-II fluorophores for mitochondria-targeted cancer imaging and photothermal therapy, Nat. Commun. 11 (2020) 6183.
[39] Y. Li, Z. Cai, S. Liu, H. Zhang, S.T.H. Wong, J.W.Y. Lam, R.T.K. Kwok, J. Qian, B. Z. Tang, Design of AIEgens for near-infrared IIb imaging through structural modulation at molecular and morphological levels, Nat. Commun. 11 (2020) 1255.
[40] B. Li, M. Zhao, L. Feng, C. Dou, S. Ding, G. Zhou, L. Lu, H. Zhang, F. Chen, X. Li, G. Li, S. Zhao, C. Jiang, Y. Wang, D. Zhao, Y. Cheng, F. Zhang, Organic NIR-II molecule with long blood half-life for in vivo dynamic vascular imaging, Nat. Commun. 11 (2020) 3102.
[41] S. Diao, J.L. Blackburn, G. Hong, A.L. Antaris, J. Chang, J.Z. Wu, B. Zhang, K. Cheng, C.J. Kuo, H. Dai, Fluorescence imaging in vivo at wavelengths beyond 1500 nm, Angew. Chem. Int. Ed. 54 (2015) 14758–14762.
[42] Y. Zhong, Z. Ma, S. Zhu, J. Yue, M. Zhang, A.L. Antaris, J. Yuan, R. Cui, H. Wan, Y. Zhou, W. Wang, N.F. Huang, J. Luo, Z. Hu, H. Dai, Boosting the down-shifting luminescence of rare-earth nanocrystals for biological imaging beyond 1500 nm, Nat. Commun. 8 (2017) 731.
[43] Y. Liu, Y. Li, S. Koo, Y. Sun, Y. Liu, X. Liu, Y. Pan, Z. Zhang, M. Du, S. Lu, X. Qiao, J. Gao, X. Wang, Z. Deng, X. Meng, Y. Xiao, J. Kim, X. Hong, Versatile types of inorganic/organic NIR-IIa/IIb fluorophores: from strategic design toward molecular imaging and theranostics, Chem. Rev. (2021), https://doi.org/10.1021/acs.chemrev.1c00553.
[44] C. Li, G. Chen, Y. Zhang, F. Wu, Q. Wang, Advanced fluorescence imaging technology in the near-infrared-II window for biomedical applications, J. Am. Chem. Soc. 142 (2020) 14789–14804.
[45] M. Zhang, J. Yue, R. Cui, Z. Ma, H. Wan, F. Wang, S. Zhu, Y. Zhou, Y. Kuang, Y. Zhong, D. Pang, H. Dai, Bright quantum dots emitting at ~1,600 nm in the NIR-IIb window for deep tissue fluorescence imaging, P. Natl. Acad. Sci. USA 115 (2018) 6590–6595.
[46] Y. Li, Y. Liu, Q. Li, X. Zeng, T. Tian, W. Zhou, Y. Cui, X. Wang, X. Cheng, Q. Ding, X. Wang, J. Wu, H. Deng, Y. Li, X. Meng, Z. Deng, X. Hong, Y. Xiao, Novel NIR-II organic fluorophores for bioimaging beyond 1550 nm, Chem. Sci. 11 (2020) 2621–2626.
[47] Q. Li, Q. Ding, Y. Li, X. Zeng, Y. Liu, S. Lu, H. Zhou, X. Wang, J. Wu, X. Meng, Z. Deng, Y. Xiao, Novel small-molecule fluorophores for in vivo NIR-IIa and NIR-IIb imaging, Chem. Commun. 56 (2020) 3289–3292.
[48] S. Liu, H. Ou, Y. Li, H. Zhang, J. Liu, X. Lu, R.T.K. Kwok, J.W.Y. Lam, D. Ding, B. Z. Tang, Planar and twisted molecular structure leads to the high brightness of semiconducting polymer nanoparticles for NIR-IIa fluorescence imaging, J. Am. Chem. Soc. 142 (2020) 15146–15156.
[49] W. Zhang, W. Deng, H. Zhang, X. Sun, T. Huang, W. Wang, P. Sun, Q. Fan, W. Huang, Bioorthogonal-targeted 1064 nm excitation theranostic nanoplatform for precise NIR-IIa fluorescence imaging guided efficient NIR-II photothermal therapy, Biomaterials 243 (2020), 119934.
[50] L. Tang, X. Zeng, H. Zhou, C. Gui, Q. Luo, W. Zhou, J. Wu, Q. Li, Y. Li, Y. Xiao, Theranostic gold nanoclusters for NIR-II imaging and photodynamic therapy, Chem. Res. Chin. U. 37 (2021) 934–942.
[51] F. Ding, C. Li, Y. Xu, J. Li, H. Li, G. Yang, Y. Sun, PEGylation regulates self-assembled small-molecule dye-based probes from single molecule to nanoparticle size for multifunctional NIR-II bioimaging, Adv. Healthcare Mater. 7 (2018) 1800973.
[52] A.L. Antaris, H. Chen, K. Cheng, Y. Sun, G. Hong, C. Qu, S. Diao, Z. Deng, X. Hu, B. Zhang, X. Zhang, O.K. Yaghi, Z.R. Alamparambil, X. Hong, Z. Cheng, H. Dai, A small-molecule dye for NIR-II imaging, Nat. Mater. 15 (2016) 235–242.
[53] Y. Zheng, Q. Li, J. Wu, Z. Luo, W. Zhou, A. Li, Y. Chen, T. Rouzi, T. Tian, H. Zhou, X. Zeng, Y. Li, X. Cheng, Y. Wei, Z. Deng, F. Zhou, X. Hong, All-in-one mitochondria-targeted NIR-II fluorophores for cancer therapy and imaging, Chem. Sci. 12 (2020) 1843–1850.
[54] H. Chen, K. Shou, S. Chen, C. Qu, Z. Wang, L. Jiang, M. Zhu, B. Ding, K. Qian, A. Ji, H. Lou, L. Tong, A. Hsu, Y. Wang, D.W. Felsher, Z. Hu, J. Tian, Z. Cheng, Smart self-assembly amphiphilic cyclopeptide-dye for near-infrared window-II imaging, Adv. Mater. 33 (2021) 2006902.
[55] A. Yuan, X. Qiu, X. Tang, W. Liu, J. Wu, Y. Hu, Self-assembled PEG-IR-780-C13 micelle as a targeting, safe and highly-effective photothermal agent for *in vivo* imaging and cancer therapy, Biomaterials 51 (2015) 184–193.
[56] Q. Yang, Z. Hu, S. Zhu, R. Ma, H. Ma, Z. Ma, H. Wan, T. Zhu, Z. Jiang, W. Liu, L. Jiao, H. Sun, Y. Liang, H. Dai, Donor engineering for NIR-II molecular fluorophores with enhanced fluorescent performance, J. Am. Chem. Soc. 140 (2018) 1715–1724.
[57] L.B. Knudsen, J. Lau, The discovery and development of liraglutide and semaglutide, Front. Endocrinol. 10 (2019) 155.
[58] A. Di, J. Schmitt, M.A. Da Silva, K. Hossain, N. Mahmoudi, R.J. Errington, Self-assembly of amphiphilic polyoxometalates for the preparation of mesoporous polyoxometalate-titania catalysts, Nanoscale 12 (2020) 22245–22257.
[59] B. Li, P. Jain, J. Ma, J.K. Smith, Z. Yuan, H. Hung, Y. He, X. Lin, K. Wu, J. Pfaendtner, S. Jiang, Affiliations expand trimethylamine N-oxide-derived zwitterionic polymers: a new class of ultralow fouling bioinspired materials, Sci. Adv. 5 (2019) eaaw9562.
[60] S. Peng, B. Ouyang, Y. Men, Y. Du, Y. Cao, R. Xie, Z. Pang, S. Shen, Biodegradable zwitterionic polymer membrane coating endowing nanoparticles with ultra-long circulation and enhanced tumor photothermal therapy, Biomaterials 231 (2020), 119680.